JOURNAL OF GEOPHYSICAL RESEARCH: OCEANS, VOL. 118, 2734–2745, doi:10.1002/jgrc.20214, 2013

Traditional quasi-geostrophic modes and surface quasi-geostrophic solutions in the Southwestern Atlantic

Cesar B. Rocha,[1,2] Amit Tandon,[2] Ilson C. A. da Silveira,[1] and Jose Antonio M. Lima[3]

Received 11 October 2012; revised 29 March 2013; accepted 19 April 2013; published 30 May 2013.

[1] We investigate whether the Quasi-geostrophic (QG) modes and the Surface Quasi-geostrophic (SQG) solutions are consistent with the vertical structure of the subinertial variability off southeast Brazil. The first-order empirical orthogonal function (EOF) of current meter time series is reconstructed using different QG mode combinations; the first EOF is compared against SQG solutions. At two out of three moorings, the traditional flat-bottom barotropic (BT) and first baroclinic (BC1) mode combination fails to represent the observed sharp near-surface decay, although this combination contains up to 78% of the depth-integrated variance. A mesoscale broad-band combination of flat-bottom SQG solutions is consistent with the near-surface sharp decay, accounting for up to 85% of the first EOF variance. A higher-order QG mode combination is also consistent with the data. Similar results are obtained for a rough topography scenario, in which the velocity vanishes at the bottom. The projection of the SQG solutions onto the QG modes confirms that these two models are mutually dependent. Consequently, as far as the observed near-surface vertical structure is concerned, SQG solutions and four-QG mode combination are indistinguishable. Tentative explanations for such vertical structures are given in terms of necessary conditions for baroclinic instability. "Charney-like" instabilities, or, surface-intensified "Phillips-like" instabilities may explain the SQG-like solutions at two moorings; traditional "Phillips-like" instabilities may rationalize the BT/BC1 mode representation at the third mooring. These results point out to the presence of a richer subinertial near-surface dynamics in some regions, which should be considered for the interpretation and projection of remotely sensed surface fields to depth.

Citation: Rocha, C. B., A. Tandon, I. C. A. da Silveira, and J. A. M. Lima (2013), Traditional quasi-geostrophic modes and surface quasi-geostrophic solutions in the Southwestern Atlantic, *J. Geophys. Res. Oceans*, *118*, 2734–2745, doi:10.1002/jgrc.20214.

1. Introduction

[2] An interesting conundrum has arisen in the scientific literature on the correct dynamics to represent the global remotely sensed sea surface height (SSH) and sea surface temperature (SST) at mesoscales and their relationship to the vertical structure of the oceanic flows [e.g., *Lapeyre*, 2009; *Ferrari and Wunsch*, 2010]. Two dynamical ideas have been invoked to extend the SSH and SST (and soon sea surface density, as surface salinity measurements from *Aquarius* [*Lagerloef et al*., 2008] become available) to subsurface: traditional quasi-geostrophic (QG) modes and surface quasi-geostrophic (SQG) solutions.

[3] The first idea stems from the work by *Wunsch* [1997], who observationally investigated the vertical partition of the horizontal kinetic energy (KE). Based on 107 moorings (mainly in the North Atlantic and Pacific oceans), this study concluded that, in general, the daily-averaged surface KE is mainly due to first baroclinic (BC1) motions. *Wunsch* [1997] argued that this is because the BC1 mode is surface intensified; consequently, altimeters may reflect this motion. This seems consistent with theoretical predictions [*Fu and Flierl*, 1980] and idealized numerical QG turbulence experiments [e.g., *Scott and Arbic*, 2007]. *Scott and Furnival* [2012] investigated further the use of a phase-locked linear combination of the barotropic (BT) and BC1 modes to extrapolate the surface geostrophic velocity. The authors pointed out that this linear combination loses predictive skills below 400 m.

[4] The second idea is based on the SQG approximation. In SQG models [e.g., *Held et al*., 1995], the flow is driven by surface buoyancy anomalies, with constant (generally zero) interior potential vorticity (PV). Indeed, the surface buoyancy anomalies can be interpreted as a delta-function PV anomaly [*Bretherton*, 1966], producing surface-intensified solutions. The appeal of the SQG framework is that the vertical solutions depend on the horizontal structure.

[1]Instituto Oceanográfico, Universidade de São Paulo, São Paulo, Brasil.
[2]University of Massachusetts Dartmouth, North Dartmouth, Massachusetts, USA.
[3]Centro de Pesquisas e Desenvolvimento Leopoldo A. Miguez de Mello, Petróleo Brasileiro S. A., Brasil.

Corresponding author. C. B. Rocha, Instituto Oceanográfico, Universidade de São Paulo, Pça do Oceanográfico, 191, Cid. Universitária, 05508-120, São Paulo, Brasil. (cesar.rocha@usp.br)

2169-9275/13/10.1002/jgrc.20214

Hence, the subsurface dynamics can be recovered solely from surface information and the mean stratification profile [e.g., *Lapeyre and Klein*, 2006]. Although the constant interior PV assumption seems to be too strong [*LaCasce*, 2012] (hereafter L12), it is remarkable that the SQG correctly predicts the flow in some regions. Comparisons against primitive-equation simulations [*Lapeyre and Klein*, 2006; *Isern-Fontanet et al*., 2008] and observations [*LaCasce and Mahadevan*, 2006] have shown that the flow resembles the SQG recovered fields, although it underestimates the velocity at depth. This problem can be partially solved by applying an adjustable constant stratification [*Lapeyre and Klein*, 2006; *Isern-Fontanet et al*., 2008] (the "effective" parameter in their terminology) or by seeking an empirical correlation between surface buoyancy and interior PV anomalies [*LaCasce and Mahadevan*, 2006].

[5] Is has also been argued that the SQG may be a better framework for the upper ocean balanced dynamics since the slope of (along-track) altimeter-derived SSH wave number spectra at mesoscales seem to be more consistent with the slope predicted by SQG turbulence theory [e.g., *Le Traon et al*., 2008] than with the slope predicted by the classical QG turbulence theory and previously used to rationalize SSH observations [e.g., *Stammer*, 1997]. However, altimeter-derived spectra slopes do not seem to match those few estimates from in situ observations [*Wang et al*., 2010], likely owing to noise contamination in altimeter measurements even at mesoscales [e.g., *Xu and Fu*, 2011, 2012].

[6] These two views of the upper ocean balanced dynamics do not exclude each other. *Ferrari and Wunsch* [2010] showed that a phase-locked linear combination between BT and BC1 modes is consistent with the SQG solution, because it can produce a surface intensification depending on the phase. L12's elegant analytical solutions show that long SQG waves project primarily onto the BT and BC1 modes, thus resembling a combination of these modes. In addition, the similarity between the BC1 mode and SQG solution is even more striking for an ocean with rough topography; the major difference is that the SQG vertical decay is slightly sharper than that of the BC1 mode.

[7] The current meter time series Empirical Orthogonal Functions (EOFs) are frequently evaluated in terms of the combinations of linear QG dynamical modes [e.g., *Kundu et al*., 1975; *da Silveira et al*., 2008]. Although L12 clarifies the connections and distinctions between QG modes and SQG solutions, these ideas have not yet been tested against observations. Here we investigate whether the SQG solutions are consistent with the vertical structure of current meter moorings statistics off southeast Brazil, and explore their similarities to the traditional QG modes. This is done by assessing the errors obtained by reconstructing the EOFs with different QG mode combination and comparing against SQG solutions. We believe that this can shed light on the interpretation and projection of surface fields (at mesoscales) as well as their projections to depth in this region, where in situ observations are limited.

[8] This paper is organized as follows. In Section 2, a brief theoretical review on the traditional QG modes and SQG solutions is presented, primarily focusing on the vertical structure. The data sets and methods used in this work are reported in section 3. Section 3.1 describes the main results of projections of the EOFs onto QG modes as well as its comparisons against the SQG solutions. Sections 3.2 and 3.3 present discussion and concluding remarks, respectively.

2. Traditional QG Modes and SQG Solutions

[9] The traditional linear QG modes and the SQG solutions arise from separation of variables of the governing equations [e.g., *Pedlosky*, 1987]. For the QG modes, the vertical structure is governed by

$$\frac{\mathrm{d}}{\mathrm{d}z}\left(\frac{f_0^2}{N^2}\frac{\mathrm{d}\phi}{\mathrm{d}z}\right)+\lambda^2\phi=0, \tag{1}$$

where ϕ is the vertical structure, f_0 and $N(z)$ are the inertial and stratification frequencies, respectively, and $-\lambda^2$ is the separation constant. At the boundaries, one generally requires [e.g., *Pedlosky*, 1987]

$$\frac{\mathrm{d}\phi}{\mathrm{d}z}=0, \text{at } z=0, z=-H. \tag{2}$$

[10] Equation (1) is derived assuming a mean motionless and linear ocean. Also, the boundary condition at $z=-H$ requires a flat bottom. These assumptions are, to some extent, violated everywhere in the ocean. In particular, in our study region, the presence of the Brazil Current and the sloping topography may affect this decomposition. Nevertheless, we treat this as a local and linear problem. Boundary conditions for rough topography are discussed in section 4.4.

[11] Equation (1) along with the boundary conditions (equation (2)) constitute a particular case of the classical Sturm-Liouville eigenvalue problem. The eigensolutions (ϕ_j) are the traditional QG modes. The eigenvalues λ_j^2 are (by definition) the inverse of the deformation radii squared.

[12] An implication of the traditional QG modes is that buoyancy anomalies are not allowed at the boundaries [e.g., L12]. Conversely, the SQG problem is posed to allow density anomalies at the surfaces [e.g., *Held et al*., 1995; *Lapeyre and Klein*, 2006; *LaCasce and Mahadevan*, 2006; *Lapeyre*, 2009]. In this case, the vertical structure is governed by

$$\frac{\mathrm{d}}{\mathrm{d}z}\left(\frac{f_0^2}{N^2}\frac{\mathrm{d}\chi}{\mathrm{d}z}\right)-K^2\chi=0, \tag{3}$$

where we follow L12's notation and change the variable for the vertical structure function to keep it different from the traditional QG modes. Also, for this case $\lambda^2=-K^2$, where $K=\sqrt{k_x^2+k_y^2}$; (k_x, k_y) is the wave number in the (x,y) direction. This follows directly from the constant interior PV assumption [L12]. The boundary conditions (assuming no buoyancy anomalies at the bottom for simplicity) are

$$\frac{\mathrm{d}\chi}{\mathrm{d}z}=1, \text{ at } z=0, \tag{4}$$

and

$$\frac{\mathrm{d}\chi}{\mathrm{d}z}=0, \text{ at } z=-H. \tag{5}$$

[13] Unlike the traditional QG modes, the SQG vertical structure $[\chi(z)]$ is intrinsically dependent on the horizontal scale (K). Therefore, equation (3) along with the boundary conditions (equations (4) and (5)) do not form an eigenvalue problem; consequently, there is a continuum of SQG solutions in case K is continuous (infinite unbounded domain).

3. Data and Methods

3.1. Current Meter Moorings

[14] Three moorings are used to estimate the vertical structure of the time-dependent flow. The MARLIM mooring (22.7° S; 40.2° W; Figure 1) is in the Brazil Current domain at the 1250 m isobath off-shore the coast of Rio de Janeiro, Brazil. It had 9 electromagnetic Marsh-McBirney sensors [50; 100; 250; 350; 450; 650; 750; 950; 1050 m]. From February 1992 to December 1992 (with an approximately 30 day-long gap in May 1992), this mooring had 308 days of hourly current measurements. The second half of this series was analyzed by *da Silveira et al*. [2008], who showed that the mooring has adequate vertical resolution to describe the mean patterns and mesoscale variability of the Brazil Current.

[15] The other two moorings analyzed in the present work come from the WOCE Experiment, as part of the German component (IFM-Kiel) of the "Deep Basin Southwestern Boundary" array. Both moorings span January 1991 through November 1992, providing about 650 days of current measurements every 2 h. The WOCE 333 mooring (27.9° S; 46.7° W; Figure 1; hereafter W333) is in the Brazil Current domain, farther south than the MARLIM mooring, at the 1200 m isobath. It had four Aanderaa RCM8 current meters [230; 475; 680; 885 m] and one upward-looking 150 kHz ADCP at about 200 m. The ADCP provides current measurements at 8 m resolution. We use seven ADCP levels [51; 77; 95; 112; 138; 155; 173 m]. The W335 mooring (28.3° S; 45.3° W; Figure 1; hereafter W335) is located off the Brazil Current at the base of the continental slope (approximately 3300 m isobath) in the domain a recirculation flow. It had six Aanderaa RCM8 current meters [275; 515; 915; 1415; 2510; 3215 m] and one upward-looking 8 m-bin 150 kHz ADCP at about 250 m. We use 7 ADCP levels [55; 72; 98; 115; 150; 192; 237 m]. While measurements within the mixed layer are available, we have not used them here, as they include a substantial component of ageostrophic motion. A detailed description of both WOCE moorings configurations and basic statistics is provided by *Müller et al*. [1998].

[16] The current meter time series are low-pass filtered using a *Lanczos* filter. The cutoff frequency is set 1/40 h^{-1} in order to retain only the subinertial energy. Additionally, the temporal mean of the filtered series is removed.

3.2. Climatological Stratification

[17] The mean stratification is needed to compute the QG modes and SQG solutions. For each mooring, the stratification is computed using annual mean temperature and salinity profiles from the *World Ocean Atlas* 2009 climatology [*Locarnini et al*., 2010; *Antonov et al*., 2010]. The eight closest profiles of the 0.25° resolution climatology are averaged (shelf profiles are excluded in the MARLIM and W333 cases). The stratification frequency is then computed, gridded in the vertical for each 10 m and smoothed following *da Silveira et al*. [2000]. The resulting profiles are shown in Figure 2.

3.3. SST Imagery

[18] SST images are used for estimating the horizontal scales necessary to compute the SQG solutions. We selected all cloud-free 7 day composite of 4 km resolution AVHRR images from Pathfinder (version 5.1, NOAA) spanning the period of the moorings. A square grid (4 km resolution) of approximately 600 km × 600 km is selected for two regions: (i) The MARLIM region; and (ii) The

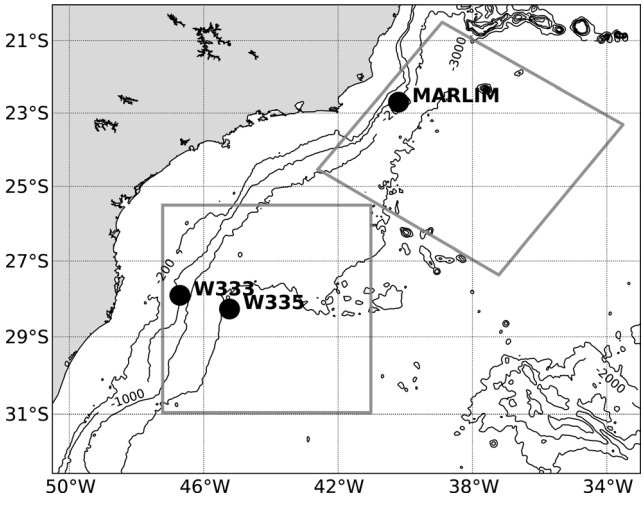

Figure 1. Mooring locations for MARLIM, W333, and W335. Solid black lines indicate the bathymetric depths. The limits of the grids used to compute the SST spectra are shown in gray.

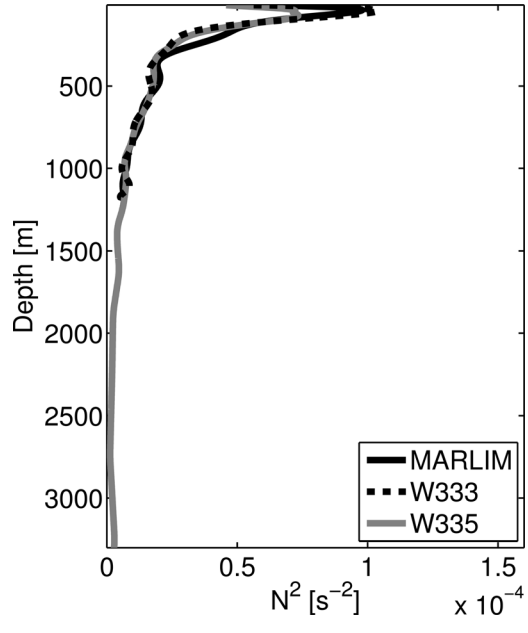

Figure 2. Climatological $N^2(z)$ profiles for MARLIM (black), W333 (dashed black) and W335 (gray) moorings region.

WOCE regions. Due to the geometrical constraints of the continental margin, the MARLIM mooring region square grid is rotated clockwise by 30° such that the zonal component is approximately a cross-isobath component. The SST from the original Pathfinder grid is linearly interpolated onto this new grid. The current meter velocity vector is rotated in a similar fashion, and hereafter the $v(u)$ component refer to the along- (cross-)isobath. Additionally, in this case, the mooring is located close to the middle of the inshore edge of the grid (Figure 1). The WOCE grid is north-south/east-west oriented. The grid is centered at the positions of the W335 mooring. The W333 mooring is located close to the eastern edge of the grid.

[19] In order to examine the existence of dominant horizontal scales, we compute the zonal and meridional mean wave number spectra. As we are interested only in the mesoscale eddies passing through the moorings, the SST images are high-pass filtered using a *Butterworth* filter. The cutoff wave number is set as 1/300 km^{-1}; half of the domain size. The SST anomalies are detrended and multiplied by a Hanning window (5 points). The fast Fourier transform is computed for a mirror symmetric domain [e.g., *Isern-Fontanet et al*., 2006, 2008]; the mean wave number spectra is then computed assuming isotropy of scales.

[20] The number of high quality cloud-free images (4 [10] for the MARLIM [WOCE] region/period) is too small to provide a statistically significant result. Hence, this spectra should be considered as a first attempt to characterize of the horizontal scales of the variability within these regions during the mooring periods. Microwave imagery is not available for the time of the moorings.

3.4. Statistical Mode Computation

[21] EOFs are used to characterize the coherent spatial (vertical) pattern of the subinertial variability as measured by the moorings. The statistical or empirical modes are indeed an orthogonal basis for the data covariance matrix [e.g., *Emery and Thomson*, 2001]. We compute the covariance matrices using the Mathworks, Inc. MATLAB® "nancov" script, that allows computing the covariance for gappy data (MARLIM mooring). The EOFs are computed by finding the eigenvalues (fraction of variance) and eigenvectors (EOF vertical structure, in this case) of the covariance matrix numerically.

[22] In order to evaluate which EOFs are statistically meaningful, we use a Monte Carlo [*Preisendorfer*, 1988] process, which consists of computing the EOFs for 100 surrogate random matrix of the same size as the data matrix; the random series are also filtered the same way as the velocity series. The amount of variance contained in each statistical mode (i.e., the relative contribution to the total energy) is then averaged; two standard deviations interval represent its 95% significance limits. Only the statistical modes above the significance limits are considered statistically meaningful.

[23] Pressure sensors records reveals significant vertical displacements during highly energetic events, particularly at the W335 mooring. For instance, the 275 m instrument (nominal depth) of the W335 mooring reached depths as deep as 550 m during one of such events. This could bias the QG mode projection specifically during such events, as discussed by *Wunsch* [1997] and *Ferrari and Wunsch* [2010]. However, as these events are short-lived, they do not significantly affect the first EOF vertical structure. Therefore, the vertical displacement of the instruments do not impact the overall results of the present study.

3.5. Dynamical Mode Fit

[24] In this work we explain the spatial (vertical) structure of variability with the traditional QG modes and SQG solutions using EOFs as a measure of variability. Although the EOFs are only a statistical measure, we assume that the subinertial variability in this region is dominated by first-order geostrophic motion. We therefore try to attribute physical meaning to the statistical modes by projecting them onto the QG modes. EOFs are also compared against SQG solutions.

[25] The fundamental decomposition used here is similar to that of the projection of the velocity profiles onto dynamical modes [e.g., *Wunsch*, 1997]. We write, in matrix notation,

$$[\mathrm{EOF}_u, \mathrm{EOF}_v] = F[A_u, A_v] + [R_u, R_v], \tag{6}$$

where $\mathrm{EOF}_{uM\times 1}(\mathrm{EOF}_{vM\times 1})$ is the dominant EOF matrix for the $u(v)$ velocity component; $A_{uN\times 1}(A_{vN\times 1})$ is the modal amplitude matrix; $F_{M\times N}$ is QG mode matrix (column 1 stands for the BT mode; columns N stands for the $N-1$th baroclinic mode); $R_{uM\times 1}(R_{vM\times 1})$ is the residual and should be considered as the sum of errors from: (i) instrument uncertainties (propagated to the EOF computation); (ii) numerical errors from the eigenvalue/eigenvector numerical algorithm; and (iii) breakdown of the assumption that the variability in this frequency band is due to QG motion.

[26] We assume that the energy is concentrated in the five gravest modes (i.e., $N=5$ in equation (6)). These QG modes are computed by solving the Sturm-Liouville problem (equations (1) and (2)) numerically given the climatological $N^2(z)$ profile. The modal amplitudes are obtained by projecting the EOFs onto the QG modes. As the system is overdetermined for all moorings (i.e., number of vertical levels greater than the number of dynamical modes), the projection is done by solving the normal equations:

$$[A_u, A_v] = \left(F^T F\right)^{-1} F^T [\mathrm{EOF}_u, \mathrm{EOF}_v]. \tag{7}$$

[27] The EOFs are reconstructed using one to five modes. The ability of the dynamical modes to represent the EOFs is evaluated by comparing the reconstructed (synthesized) profile against the statistical modes. A statistical measure of this comparison is the normalized RMS difference:

$$[\mathrm{RMS}_{u\mathrm{diff}}, \mathrm{RMS}_{v\mathrm{diff}}] = \frac{||[\mathrm{EOF}_u, \mathrm{EOF}_v] - F^j\left[A_u^j, A_v^j\right]||}{||[\mathrm{EOF}_u, \mathrm{EOF}_v]||}, \tag{8}$$

where the vertical bars denote the length and j is the number of modes used for a particular reconstruction (synthesis). For example, we reconstruct the EOF using a BT/BC1 mode combination by setting $j=2$ ($A_u^2 = A_{u2\times 1}$ and $F^2 = F_{M\times 2}$). The $\mathrm{RMS}_{\mathrm{diff}}$ using five modes ($j=5$) should be a measure of the residual (R). Furthermore, the

complement of equation (8) (i.e., $1 - \mathrm{RMS}_{\mathrm{diff}}$) is the fraction of the EOF variance accounted for by the QG mode synthesis.

3.6. SQG Versus First EOF

[28] As the SQG vertical solution depends on the horizontal scales, we estimate the dominant wavelengths by computing the mean wave number spectra using the set of AVHRR images described above. The mean SST wave number spectrum for the W333 and W335 region is shown in Figure 3. The spectrum is broad-banded at mesoscales (from ≈50 km up to the cutoff wavelength). It has high uncertainty owing to the small number of cloud-free images, making these results a rough estimate. Consequently, no dominant wave number could be identified. (The spectrum for the MARLIM mooring (not shown) region is similar.) Thus, the SQG vertical structure is computed as a combination of all the waves resolved in the spectrum. That is, in the physical space we write

$$\overline{\chi}(z) = \sqrt{\sum_{i=1}^{N} |\hat{V}|^2 \chi^2(K_i, z)}, \qquad (9)$$

where the hatted quantity stands for the Fourier transform of the respective variable. In deriving equation (9), we used the Parseval's theorem. Note that, in the SQG framework, the velocity (kinetic energy) spectrum is related to the SST spectrum (assuming SST anomalies are representative of density variations): $|\hat{V}|^2 = |\hat{u}|^2 + |\hat{v}|^2 \propto \chi^2(K_i, z = 0) K_i^2 |\hat{T}|^2)$. Therefore, under this approach, either surface velocity or temperature measurements could be used to estimate $\overline{\chi}(z)$. Since our mooring data are prior to the multi-altimeter-derived geostrophic velocity era, we use SST data.

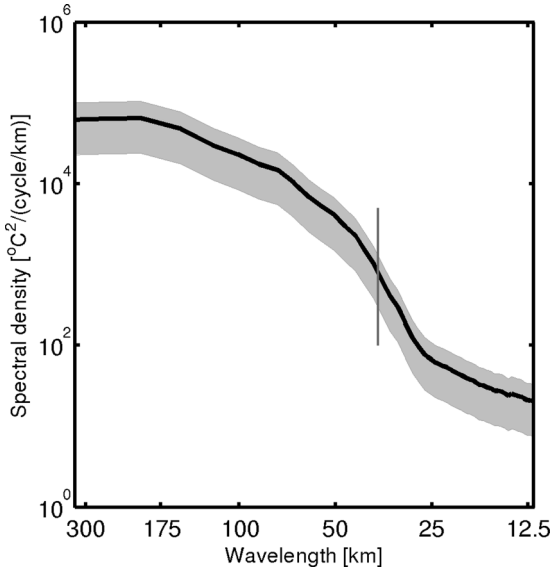

Figure 3. SSTa spectrum (black line) for W333 and W335 moorings region. The gray shadow represents the 95% confidence interval. For reference, the gray vertical line indicates the first baroclinic deformation radius (33 km) for W335 mooring region.

[29] For each wave number, we compute the SQG vertical structure [i.e., $\chi(K_i, z)$] by solving numerically the SQG vertical problem (equation (3) subject to equations (4) and (5)) given the climatological $N^2(z)$ profile; the combination of SQG vertical structures of all resolved wave numbers (equation (9)) provides the SQG solution $[\overline{\chi}(z)]$ that is ultimately compared against the first EOF vertical structure. As it accounts for a range of wavelengths, we think this combination is a better way of representing the SQG solution for comparing it with the EOFs vertical structure.

[30] Another method for combining the SQG waves was also tested, namely simply combining the SQG solutions weighted by the energy fraction in each wave number resolved in the SST spectrum. This linear combination produces SQG solutions (not presented) very similar to those obtained with equation (9). Another (more arbitrary) possibility is to look for which wave number produces the SQG solution that best fits the first EOF vertical structure. The results (not presented) point that wavelengths of 250–300 km best fit the data; these vertical structures do not significantly differ from the combination of SQG waves. This suggests that the summation in equation (9) is dominated by the largest wavelength, which has the highest energy fraction, although it does not represent a statistically significant peak in the spectrum.

[31] In order to be compared against the unitless EOF vertical structure, the SQG solution $[\overline{\chi}(z)]$ and the first EOF are normalized by their respective value in the depth associated to the uppermost current meter position (i.e., closest to the surface). The measure of the variance of the vertical structure of the EOF accounted for by the SQG solution is calculated using a similar criterion as in the QG mode synthesis (equation (8)).

4. Results

[32] Table 1 presents the results from EOF computations. For all moorings and both velocity components, only the first EOF is statistically significant. Therefore, hereafter we just comment on the dominant statistical mode (first EOF) for the three moorings. In general the first EOF accounts for about 85–95% of the depth-integrated variance. As there are small differences between the two components, we arbitrarily choose to focus the description of the results on the *v* component, although, the results for both components are tabulated (Tables 2 and 3) and the *u* component results for the rough topography scenario are illustrated in Figures 7–9. Significant differences are mentioned and discussed below.

4.1. EOFs Projection Onto QG Modes

[33] The results from QG mode synthesis to the first EOF are presented in Table 2. We do not present the results

Table 1. Percent of Variance Accounted for by the First Empirical Mode[a]

	First EOF_v	First EOF_u
MARLIM	83.4% ± 11.8%	81.8% ± 11.8%
WOCE 333	92.2% ± 10.6%	96.2% ± 10.6%
WOCE 335	89.6% ± 8.9%	94.4% ± 8.9%

[a]EOF_v (EOF_u) stands for the *y*- (*x* direction) velocity component EOF.

Table 2. Percent of the First (EOF_u) Depth-Integrated Variance Accounted for by One QG Mode (BT), Two QG Modes ($BT+BC_1$), and Four QG Modes ($BT+BC_1+BC_2+BC_3$), and SQG Solution[a]

	QG Mode Combination			
	One Mode	Two Modes	Four Modes	SQG
MARLIM	29.1 (27.2)%	77.8 (85.8)%	91.2 (88.6)%	82.5 (73.3)%
WOCE 333	42.8 (32.3)%	91.0 (89.5)%	94.8 (94.9)%	73.9 (77.5)%
WOCE 335	25.4 (22.8)%	69.1 (79.7)%	98.5 (97.6)%	85.0 (77.6)%

[a]The traditional flat bottom boundary condition is applied in this case.

for the five-mode combination (i.e., including the fourth-baroclinic mode), as it accounts for less than 2–3% of the first EOF depth-integrated variance at all moorings. For the MARLIM mooring, a linear combination of the BT and BC1 modes accounts for 77.8% of the depth-integrated variance. This mode combination particularly fails to capture the sharp vertical decay in the upper 300–400 m (Figure 4). Consequently, higher-order baroclinic modes are necessary to account for this near-surface variance. The BC2 and BC3 modes together contain 13.4% of the variance. These results are quite similar to those obtained by *da Silveira et al*. [2008] for the same mooring, though the series analyzed in the present work is 120 days longer. Indeed, if the time series is split in 3 month pieces and the EOFs are computed, we notice that the vertical structure of the first EOF does not change significantly. This supports the assumption that the first EOF is dominated by mesoscale variability.

[34] The projections are different for the *u* component (cross isobath in this case) for the MARLIM mooring. The BT and BC1 (see Table 2) accounts for 85.8% of the variance. This suggests some anisotropy of the variability, possibly constrained by the sloping topography.

[35] The BT/BC1 mode combination seems to better represent the first EOF vertical structure at the W333 mooring (Figure 5; see also Table 2). The linear combination of these modes contains 91.0% of the variance. Note that in this case the first EOF does not show a sharp decay in the upper 300–400 m. Thus, the BC1 mode describes the near-surface structure fairly well. The BC2 and BC3 modes together account for 3.8% of the variance.

[36] Offshore of the Brazil Current domain, at the W335 mooring, BT and BC1 modes together account for 69.1% of the first EOF variance (Figure 6; Table 2). In particular,

Table 3. Percent of the First EOF_v (EOF_u) Depth-Integrated Variance Accounted for by One QG Mode (BC_1), Two QG Modes ($BC_1+BC_2+BC_3$), and Three QG Modes ($BC_1+BC_2+BC_3$), and SQG Solution[a]

	QG Mode Combination			
	One Mode	Two Modes	Three Modes	SQG
MARLIM	67.9 (73.6)%	88.0 (90.0)%	92.8 (90.4)%	84.8 (77.1)%
WOCE 333	89.5 (82.3)%	93.3 (95.4)%	96.4 (99.2)%	68.2 (74.9)%
WOCE 335	60.2 (64.1)%	75.4 (86.6)%	95.9 (97.3)%	84.9 (84.9)%

[a]The rough topography boundary condition is applied in this case. The BT mode vanishes.

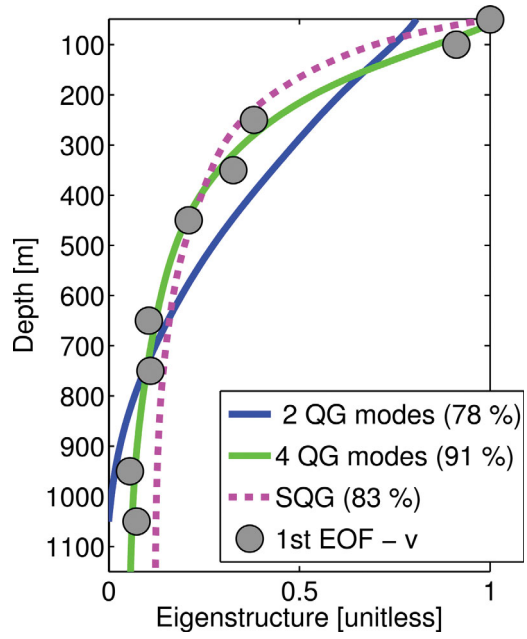

Figure 4. First EOF (filled circles) of the velocity anomalies for MARLIM mooring. Comparison against two QG modes ($BT+BC_1$) and four QG modes ($BT+BC_1+BC_2+BC_3$), and SQG solution for a flat-bottom scenario.

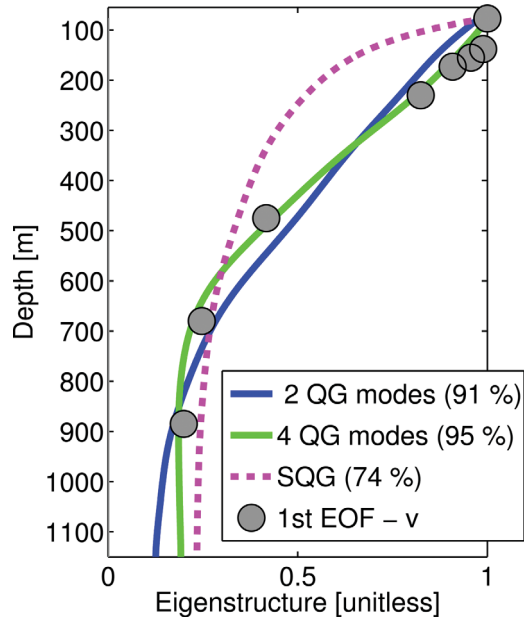

Figure 5. First EOF (filled circles) of the velocity anomalies for W333 mooring. Comparison against two QG modes ($BT+BC_1$) and four QG modes ($BT+BC_1+BC_2+BC_3$), and SQG solution for a flat-bottom scenario.

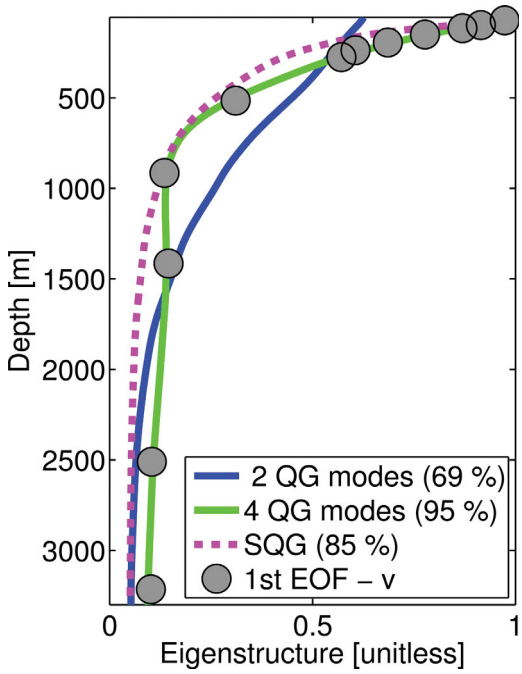

Figure 6. First EOF (filled circles) of the velocity anomalies for W335 mooring. Comparison against two QG modes ($BT+BC_1$) and four QG modes ($BT+BC_1+BC_2+BC_3$), and SQG solution for a flat-bottom scenario.

it is clear that the BC1 mode fails to represent the sharp vertical decay in the upper 500 m. Higher modes are needed to account for this variance; BC2 and BC3 modes together contain 29.6% of the variance.

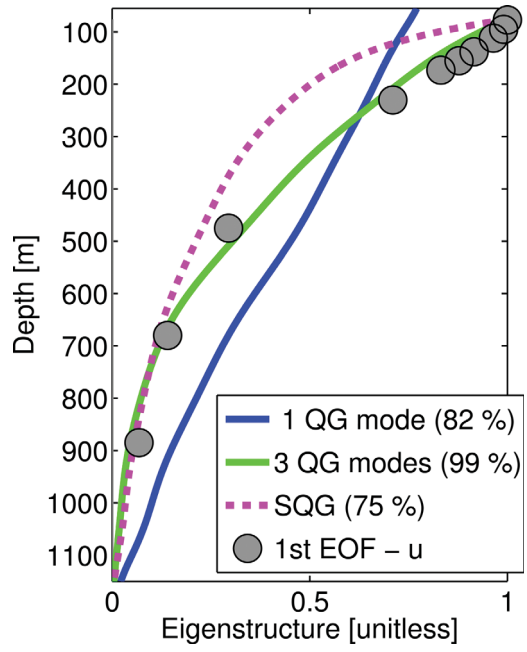

Figure 8. First EOF (filled circles) of the velocity anomalies for W333 mooring. Comparison against one QG mode (BC_1) and three QG modes ($BC_1+BC_2+BC_3$), and SQG solution for a rough topography scenario. (The BT mode vanishes in this case).

[37] The results from the MARLIM and W335 moorings are not consistent with the overall results from *Wunsch* [1997], who has shown that the bulk of the near-surface energy is accounted for by the BC1 mode. In particular, the

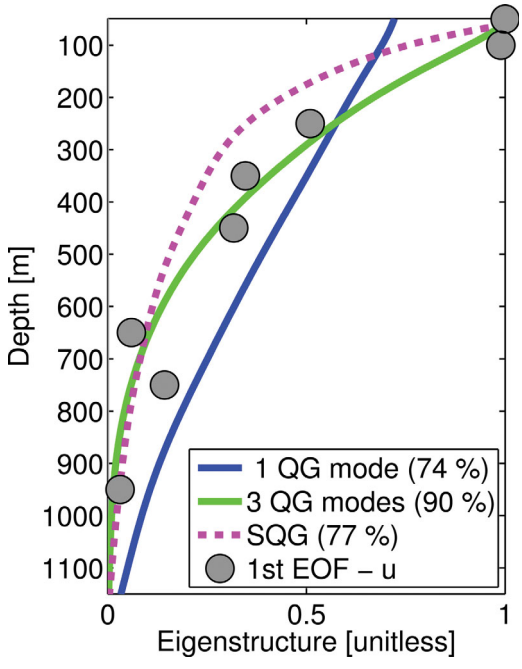

Figure 7. First EOF (filled circles) of the velocity anomalies for MARLIM mooring. Comparison against one QG mode (BC_1) and three QG modes ($BC_1+BC_2+BC_3$), and SQG solution for a rough topography scenario. (The BT mode vanishes in this case).

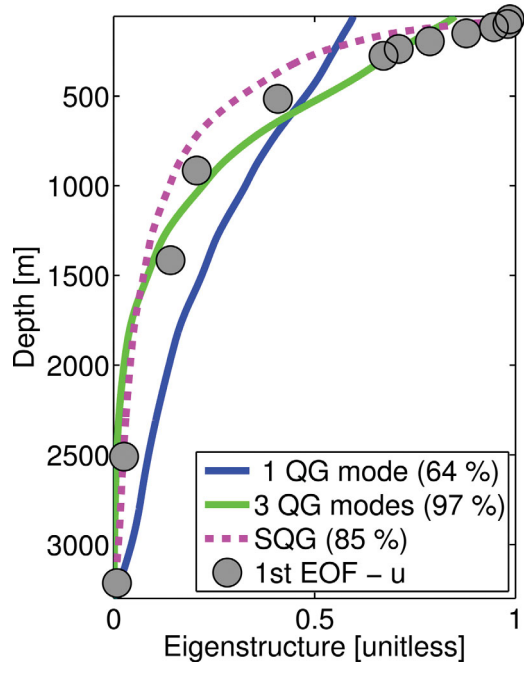

Figure 9. First EOF (filled circles) of the velocity anomalies for W335 mooring. Comparison against one QG mode (BC_1) and three QG modes ($BC_1+BC_2+BC_3$), and SQG solution for a rough topography scenario. (The BT mode vanishes in this case).

near-surface energy of these moorings contain considerable amount of energy in the BC2 and BC3 modes. These outcomes motivated us to test whether SQG solutions would be a better model for the vertical structure of the variability in these regions. As pointed out by L12, the fact that a dominant EOF in a particular region decays more sharply than the BC1 mode "could be an indication of SQG motion."

4.2. EOFs Versus SQG Solutions

[38] The results from comparisons of first EOF against the resulting SQG solution $[\overline{\chi}(z)]$ for each mooring are presented in Table 2. For the Marlim mooring (Figure 4), the SQG solution accounts for 82.5% of the first EOF variance. In particular, the SQG solution seems consistent with the sharp vertical decay in the upper 300–400m. The *u* component (cross isobath in this case) is significantly different; the SQG accounts for 73.3% of the first EOF variance in this case.

[39] For the W333 mooring (Figure 5; see also Table 2), the SQG solution contains 73.9% of the variance. However, the SQG solution vertical decay is much sharper, and it diverges dramatically from the first EOF in the upper 300–400 m. This is to be expected since the first EOF vertical structure is well represented by the BT/BC1 mode combination.

[40] For the W335 mooring (Figure 6), the SQG solution accounts for 85.0% of the first EOF variance. Unlike the BT/BC1 linear combination, the SQG solution does account for the sharp decay in the upper 500 m. The *u* component contains 77.6% of the first EOF variance. In particular, the first EOF vertical structure goes almost to zero below 2500 m, which may be an indication of effects of topography, or, bottom friction (see discussion in section 4.4).

4.3. SQG Projection Onto QG Modes

[41] As the traditional linear QG modes are solutions of the Sturm-Liouville problem (equations (1) and (2)), they constitute an orthogonal basis for the subspace of solutions. Therefore, the SQG solutions project onto them [*Ferrari and Wunsch*, 2010, L12]. Following L12, we evaluate how the SQG solutions project onto the QG modes. (Other authors treat the QG traditional mode decomposition as incomplete. They argue that they are degenerate with respect to the upper boundary condition; a good discussion is provided by *Lapeyre* [2009].)

[42] The projection results for all moorings are presented in Table 4. For the MARLIM mooring, the SQG solution projects primarily onto the BT and BC1 modes (43.6% and 33.2%, respectively), followed by the BC2 mode (14.8%) and the BC3 mode (6.0%). For the W333 mooring, the SQG solution projects primarily onto the BT mode (56.5%), followed by the BC1 mode (28.8%). This suggests that the SQG solution contains a considerable amount of the variance of the first EOF in this region, owing to the variability in this region being significantly barotropic (Figure 5). The projection of the SQG onto the higher modes (11.7% for the BC2) is consistent with the fact that the SQG solution is not consistent with the first EOF. For the W335 mooring, the SQG solution projects primarily onto the BC1 mode (34.75%), followed by the BT mode (30.5%). Considerable amount of energy is also found in the BC2 and BC3 modes (17.5% and% 11.1%, respectively).

Table 4. Projection of SQG Solution Onto QG Modes Using the Flat Bottom (Rough Topography) Boundary Condition

	Mode			
	BT	BC_1	BC_2	BC_3
MARLIM	43.6%	33.2 (56.9)%	14.8 (25.9)%	6.0 (10.7)%
WOCE 333	56.5%	28.8 (65.7)%	11.7 (24.7)%	2.9 (8.8)%
WOCE 335	30.5%	34.75 (50.7)%	17.5 (23.6)%	11.1 (12.9)%

[43] In general these projection results are in agreement with the theoretical cases studied by L12, which showed that long SQG waves project primarily onto the BT and BC1 modes, with the dominance of one or the other depending upon the decay of the stratification profile. Indeed, the WOCE 355 case is similar to the theoretical "longwave/shallow thermocline" case discussed by L12, projecting primarily onto the BC1 and BT modes, although a significant fraction of energy is found in the BC2 and BC3 modes.

4.4. The Rough Topography Scenario

[44] So far we have considered the traditional linear QG modes and the SQG solutions in a classical flat-bottom fashion, which implies no vertical velocity at the bottom, and, consequently, no buoyancy variations are allowed. (Mathematically, this is expressed by a homogeneous Neumann bottom boundary condition for the vertical structure, that is, $\mathrm{d}\phi/\mathrm{d}z = 0$ at $z = -H$.) In a more realistic scenario, with topography and bottom friction, the vertical velocity is not zero at the bottom [e.g., *Vallis*, 2006; *Ferrari and Wunsch*, 2010]. Here we investigate how topography affects the vertical structure of the QG modes and SQG solution and its comparison against the first EOF. For simplicity, we neglect the bottom friction. This would be the case when low stratification at the bottom and relatively small viscosity combine to produce a negligible friction forcing term [*Ferrari and Wunsch*, 2010]. The linearized bottom boundary condition in terms of the vertical structure becomes

$$\frac{c_y f_0}{N^2}\frac{\mathrm{d}\phi}{\mathrm{d}z} - \frac{\mathrm{d}\eta_b}{\mathrm{d}x}\phi = 0, \quad \text{at} \quad z = -H, \tag{10}$$

where ϕ is the vertical structure (although we are using the QG modes notation, the same boundary condition will be used for the SQG solution, substituting ϕ for χ); for simplicity, we considered that the topography only varies in the x direction (i.e., the departure from the mean depth is $\eta_b = \eta_b(x)$; x being approximately the cross isobath direction); c_y is the phase speed of the QG/SQG waves in the y direction. Equation (10) is a mixed boundary (Dirichlet/Neumann) condition and as it depends on the wave number ($c_y = c_y(l)$, where l is the y direction wave number), the Sturm-Liouville problem does not hold; the QG modes are not orthogonal [e.g., *Szuts et al.*, 2012]. L12 computed the QG modes and SQG solutions for two extreme cases in which the Sturm-Liouville problem holds: the classical flat bottom ($\mathrm{d}\phi/\mathrm{d}z = 0$) and rough topography ($\phi = 0$). It is interesting to evaluate the limits in which the homogeneous Dirichlet boundary condition ($\phi = 0$) could be applied. Assuming the allowable error to be 10% we could apply the Dirichlet condition provided

$$c_y \leq 0.1\frac{N^2|_{-H}H|\frac{\mathrm{d}\eta_b}{\mathrm{d}x}|}{|f_0|}. \tag{11}$$

Table 5. The Estimated Limit for Along-Isobath Phase Speed c_y for the Dirichlet Boundary Condition (Rough Topography) to Hold

	Dirichlet ($c_y \leq$ [m s^{-1}])
MARLIM	0.33
WOCE 333	0.22
WOCE 335	0.26

[45] We estimate the right-hand side of Equation (11) for the three moorings. The topographic gradient was estimated from the ETOPO2 data base and H is taken to be the mooring local depth. Generally for the three mooring regions, the Dirichlet boundary condition holds for waves with phase speeds smaller than 0.2–0.3 m s^{-1} (Table 5). Estimates for phase speeds within these regions are rare. *da Silveira et al*.'s [2008] analysis of baroclinic instability for the MARLIM mooring region suggests phase speeds of approximately 0.05 m s^{-1} for the most unstable Brazil Current baroclinic waves. Therefore, in this case, the Dirichlet boundary condition should be applied. Indeed our scaling arguments point out that the classical flat-bottom QG modes would hold only for much gentler slopes (reciprocal of equation (11)). Hence, in these three cases, the Dirichlet boundary condition (rough topography) may be a better approximation than the classical flat bottom boundary condition.

[46] A high-bottom friction regime would also lead to a homogeneous Dirichlet bottom boundary condition ($\phi = 0$). This does not seem to be the case since the first EOF of the cross-isobath component is also affected above the bottom; for instance, the cross-isobath eigenstructure for the W335 mooring almost vanishes at 2500 m depth (Figure 9), suggesting that the effect is not restricted to a boundary layer. Near-bottom horizontal velocity intensification occurs, e.g., in regions with closed f/h (where $h = H + \eta_b$ is the total depth) contours [e.g., *Dewar*, 1998], but the topography is almost meridionally oriented off Brazil. Furthermore, as this near-bottom variability is likely not coherent to that of the surface-intensified mesoscale eddies in this region, this effect would not be present in the first EOF.

[47] We recompute the QG modes as well as the SQG solutions using this new bottom boundary condition (Table 3; Figures 7–9). The rough topography seems to make the interpretation of the first EOF in terms of baroclinic modes worse. (Note that the BT mode vanishes in this case [L12].) In general, the representation close to the bottom, particularly for the x component (Figure 9) is improved. For the MARLIM mooring, the BC1 mode just contains 67.9% of the first EOF variance (compared to 77.8% of the BT/BC1 linear combination for the flat bottom case). Similarly, for the W335 mooring the BC1 mode is inadequate, accounting for only 60.2% of the first EOF variance (compared to 69.1% of the BT/BC1 flat bottom case). For the W333 case the BC1 mode contains 89.5% of the first EOF variance (compared to 91.0% of the BT/BC1 flat bottom case).

[48] On the other hand, the SQG solution still seems to be a fair model to represent the first EOF at the MARLIM and W335 moorings. The SQG solution is modified only close to the bottom and remains consistent with the data, accounting for 77.1% (84.9%) of the (x component) first EOF variance at the MARLIM (W335) mooring. In particular, the near-surface portion of the SQG solution is not significantly affected by the rough topography. Therefore, the SQG solutions remain a better model (as compared to the BT/BC1 combination) to represent the sharp decay observed in the MARLIM and W335 moorings (Figures 7 and 9).

[49] The SQG solutions project primarily onto the BC1 for the rough topography scenario. At the W333 mooring, the BC1 accounts for 65.7% of the variance; the BC2 and BC3 modes contain 24.7% and 8.8% of it, respectively. For the W335 (MARLIM) mooring, the BC1 mode contains 50.7% (56.9%) of the variance. A significant amount of energy is found in the BC2 and BC3 modes, which account for 23.6% (25.9%) and 12.9% (10.7%) of the first EOF variance, respectively.

5. Summary and Discussion

[50] We test two dynamical models of vertical structure (traditional QG modes and SQG solutions) against first EOF from two moorings in the Brazil Current domain (MARLIM and W333) and one farther offshore (W335). Traditionally, these EOFs are interpreted as a phase-locked BT and BC1 mode linear combination. However, this linear combination poorly captures the sharp decay observed in the upper 500 m (300 m) at the W335 (MARLIM) mooring, albeit it contains 69.6% (77.8%) of the depth-integrated first EOF variance. Conversely, at the W333 mooring, which does not exhibit a near-surface sharp decay, the BT/BC1 linear combination is a better representation and contains 91.0% of the first EOF variance.

[51] The second model of the vertical structure is a combination of SQG waves. The vertical decay of this SQG solution is consistent with the statistics of the variability at the W335 mooring. For this mooring, it accounts for 85.0% of the depth-integrated variance and, in particular, captures the exponential decay in the upper 500 m. To some extent, similar results were obtained for the MARLIM region. In this case, the SQG solution accounts for 82.5% of the first EOF vertical structure. However, the SQG solution presents a sharp decay which is inconsistent with the observed variability at the W333 mooring.

[52] *Ferrari and Wunsch* [2010] argue and present some mooring-based evidence that a phase relationship between BT and BC1 modes is consistent with the SQG solution. This does not seem to be true for the W335 and the MARLIM moorings. The phase-locked combination between BT and BC1 mode produces just part of the surface intensification; it does not account for the sharp vertical decay observed in this region.

[53] *Lapeyre* [2009], analyzed numerical model results from the *Parallel Ocean Program* model in the North Atlantic, and concluded that the SQG solution dominates the upper 600 m in the Gulf Stream region. The results for the W335 mooring and, to some extent, MARLIM mooring are consistent with this. However, we recognize that the SQG solutions project onto the QG modes, and another explanation for the sharp decay is simply a richer baroclinic

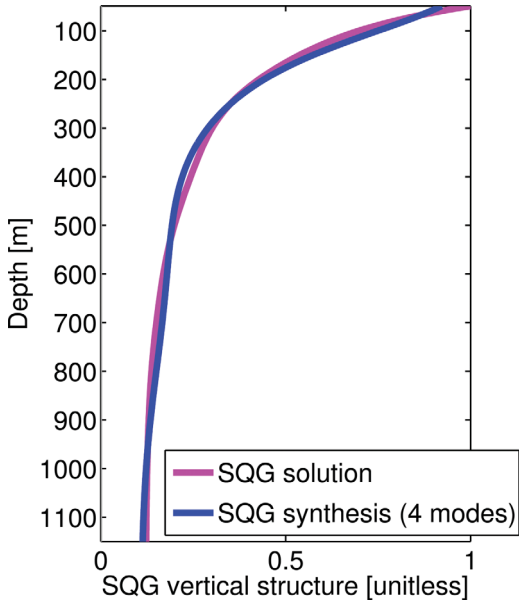

Figure 10. Flat-bottom SQG solution and its synthesis in terms of four QG modes (BT+BC_1+BC_2+BC_3) for MARLIM mooring. The synthesis accounts for 95% of the depth-integrated SQG solution variance.

composition. Indeed, this is not inconsistent with the SQG solution model if one considers that the traditional QG modes span the subspace of solutions. The projection of the SQG solutions onto the QG modes is in agreement with this: Considerable energy in the higher-baroclinic modes (BC2 and BC3) to account for the sharp decay in the upper 500 m. For instance, Figure 10 depicts the flat-bottom SQG solution for the MARLIM mooring and its synthesis using four QG modes. This synthesis accounts for 95.0% of the depth-integrated SQG solution variance. Results for the WOCE 335 mooring are very similar, where the four-QG mode synthesis accounts for 85.0% of the depth-integrated SQG solution variance, particularly representing the sharp near-surface decay. This is consistent with the fact that the inclusion of the BC2 and BC3 allows for the QG modes to account for up 98.5% of the first EOF variance. Consequently, as far as near-surface decay is concerned, SQG solutions and four-QG mode combination are indistinguishable. In other words, the SQG solution converges to a four-QG mode representation and both are consistent with the data.

[54] The calculations are repeated for a rough topography scenario, in which the velocity vanishes at the bottom. In general, the rough topography does not improve the results when trying to interpret the first EOF on the basis of the traditional QG mode. On the other hand, the SQG solution only changes close to the bottom, and still accounts for the sharp vertical decay. In particular, the SQG solutions (and higher-order QG mode combination) for rough topography better matches the first EOF for the x component. Additionally, in line with L12, the results show that for a rough topography, the similarity between the BC1 mode and SQG is higher, although higher-order QG modes are necessary to account for the near-surface sharp decay.

[55] The consistency between the SQG solutions and the first EOF vertical structure implies that SQG-based methods for reconstructing the subsurface dynamics [e.g., *Lapeyre and Klein*, 2006; *LaCasce and Mahadevan*, 2006; *Isern-Fontanet et al*., 2008] are likely to work, provided that the surface KE is matched. A natural question is whether these methods would represent the correct physics, that is, if the SQG dynamics is dominant in these regions. To answer this question, we evaluate whether the SQG solutions can account for the amplitude of the observed eddy field. We estimate the surface velocity for the SST snapshots following the SQG methodology, assuming that the surface density is dominated by SST gradients[e.g., *LaCasce and Mahadevan*, 2006]. The lateral SST gradient predicts eddy amplitudes (here defined as the spatial root mean square (RMS) of the velocity field) of about 0.07 and 0.02 m s^{-1} at the MARLIM and W335 regions, respectively. This represents only about 20% of the RMS of the uppermost velocity measurements at these moorings. Although the spatial RMS of the snapshot may not be directly comparable to the temporal RMS in a single location, these estimates are (at least) suggestive of a more complex (surface/interior) eddy dynamics. Indeed, the surface-intensified stratification affects the penetration of SQG waves, reducing its magnitude even at the surface (L12). In addition, the constant interior PV assumption is not strictly valid in these regions. The presence of the vertical shear of the Brazil Current (MARLIM and W333) and of a recirculation flow (W335) is associated with interior PV gradients. Therefore, it is likely that these SQG-like vertical structures are a combination of the surface buoyancy gradients and the surface-intensified interior PV. Nonetheless, it is remarkable that the SQG solutions correctly represent the sharp vertical decay at the MARLIM and W335 moorings.

[56] How can one explain such SQG-like vertical structures? An explanation could be sought on the basis of necessary conditions for baroclinic instability. Specifically, the relative importance of surface and interior contributions depends on the velocity vertical shear near the surface [*Lapeyre*, 2009], and this may determine the type of instability that is taking place [e.g., *Pedlosky*, 1987]. Although *Lapeyre* [2009] argues that local linear baroclinic instability does not fully explain the differences in interior/surface mode decomposition in the North Atlantic, arguments based on the Charney-Stern-Pedlosky criterion for linear baroclinic instability [e.g., *Vallis*, 2006] seem to provide a consistent explanation for the present results. In particular, the vertical shear of the long-term mean flow is intensified close to the surface at the MARLIM and W335 moorings (Figures 11 and 13), producing a long-term mean PV gradient that presents a relatively shallow zero-crossing. (Under the local approximation, we neglect the contribution of the relative vorticity in the PV. This seems a consistent approximation for the study of mesoscale phenomena [*Tulloch et al*., 2011].) The interaction of the surface shear with the PV gradient in the interior could lead to the development of Charney-like instabilities [*Tulloch et al*., 2011], producing a SQG-like vertical structure. (Here as background flow is meridional, the condition for the Charney-like instability is that the surface vertical shear has the same sign of the zonal PV gradient somewhere in the interior [e.g., *Isachsen*, 2011].) The conditions for "shallow" Phillips-like instabilities [*Tulloch et al*., 2011] are also satisfied. This would be the case in which the SQG-like vertical structure is solely

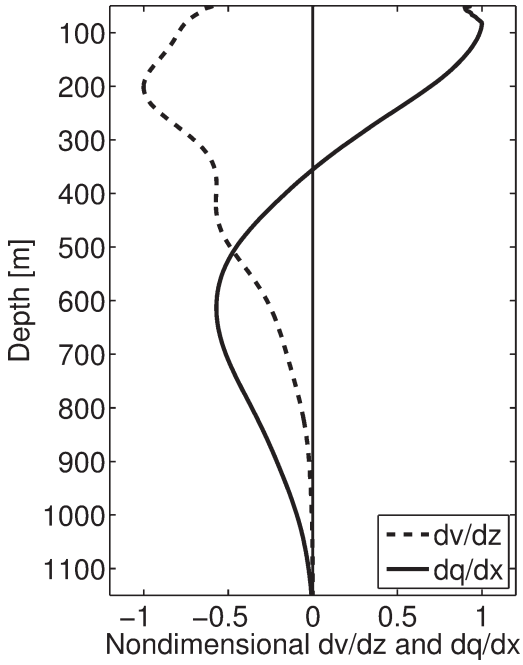

Figure 11. Mean y component velocity vertical shear (dashed line) and mean PV x component gradient (continuous line) for MARLIM mooring. The shear and PV gradient are normalized by their maximum magnitudes 1.3 10^{-3} (s^{-1}) and 4.9 10^{-10} (m^{-1} s^{-1}), respectively.

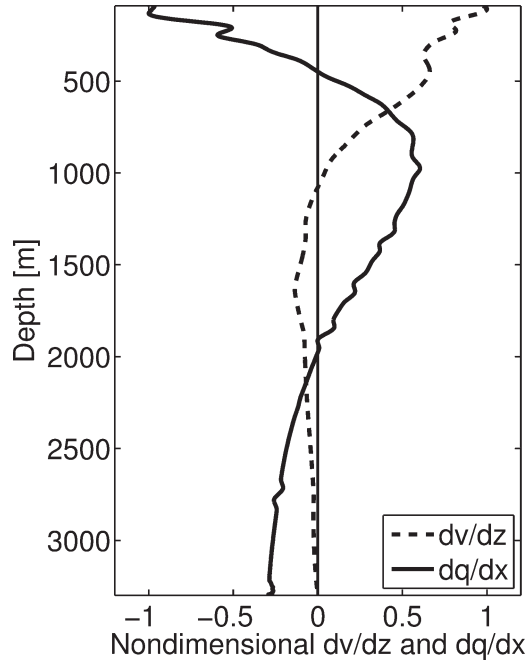

Figure 13. Mean y component velocity vertical shear (dashed line) and mean PV x component gradient (continuous line) for W335 mooring. The shear and PV gradient are normalized by their maximum magnitudes 6.5 10^{-5} (s^{-1}) and 3.8 10^{-11} (m^{-1} s^{-1}), respectively.

generated by the surface-intensified PV (without surface buoyancy variations at the surface).

[57] In contrast, the shear at the W333 mooring is intensified at mid-depth (Figure 12), producing a deeper (as compared to the MARLIM and W335 moorings) zero-crossing in the PV gradient profile. In this case, it is likely that Phillips-like instabilities [*Tulloch et al*., 2011] take place, consistent with the fact that the vertical structure of the first EOF is captured by a linear combination of two QG modes. These explanations for the observed structure are tentative, as it is difficult to accurately estimate the shear at the surface owing to the lack of instruments. In addition, it is likely that both Charney-like and Phillips-like instabilities are important. It is also well-known that the local linear baroclinic instability analysis "ignores many other dynamical possibilities" [*Tulloch et al*., 2011]. Furthermore, forced solutions could also be important; indeed, the negative equivalent depth modes [e.g., *Philander*, 1978] have SQG-like vertical structures. Therefore, the vertical structure may be a response to much more complicated surface/near-surface processes. Notwithstanding these caveats, the local linear QG baroclinic instability arguments seem to plausibly rationalize the results obtained here.

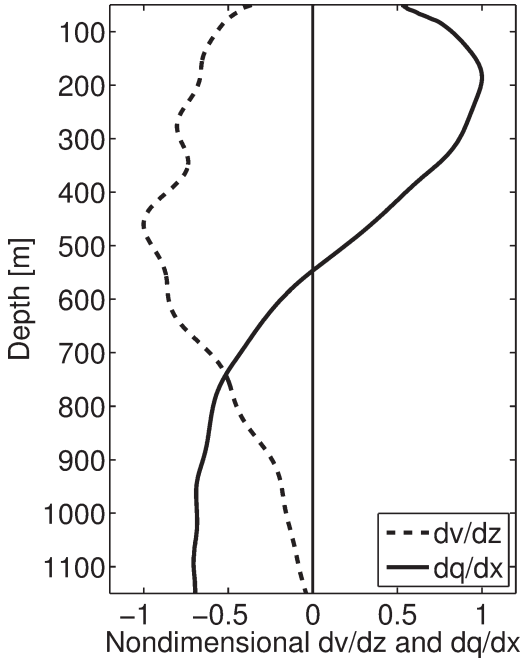

Figure 12. Mean y component velocity vertical shear (dashed line) and mean PV x component gradient (continuous line) for W333 mooring. The shear and PV gradient are normalized by their maximum magnitudes 6.0 10^{-4} (s^{-1}) and 4.4 10^{-10} (m^{-1} s^{-1}), respectively.

6. Concluding Remarks

[58] The present work shows that the SQG solution is consistent with the vertical structure of the first EOF at two (one in the Brazil Current domain and one offshore) out of the three moorings analyzed. In particular, the SQG solution can account for the observed sharp near-surface decay. However, the only conclusion we can reach is that the SQG is a better model than the traditional BT/BC1 linear combination in representing the vertical structure of the statistics of mesoscale variability in these regions, specifically its near-surface sharp decay. Nevertheless, our results point

out to the presence of a more complicated near-surface structure. On a regional scale, this implies that care should be taken in interpreting altimeter data only as due to first BC mode motions. Although an SQG interpretation or simply a richer baroclinic mode composition are both consistent with the data, the observed vertical structures may be the response to much a more complicated surface/near-surface processes. SQG-based models to recover subsurface fields are likely to correctly represent the flow in these regions, although the interior PV is clearly not constant. Regions where the main PV gradients are confined to the surface tend to present a SQG-like vertical structure. In fact, this is simply a generalization of the PV sheet argument [*Bretherton*, 1966] to a surface-trapped PV. Future work should combine global mooring data set, SSH and SST observations, and realistic numerical simulations to further investigate these issues, and consider local linear baroclinic instability analysis to rationalize the results.

[59] **Acknowledgments.** We thank three anonymous reviewers for their comments. Reviewer #2 suggested the use of baroclinic instability arguments to better understand the results. Reviewer #3 suggested a more physical combination of SQG waves (equation (9)), and we appreciate his/her insistence on this point. C. B. Rocha acknowledges the support from *Sao Paulo Research Foundation* (FAPESP, Brazil; grants 2010/13629-6 and 2012/02119-2); A. Tandon is supported by NASA (grant NNX10AE93G); I. C. A. da Silveira acknowledges CNPq (grants 474409/2008-2 and 307122/2010-7). Thanks to WOCE "ACM12 Array" PIs for making the mooring data publicly available. The MARLIM data set was kindly provided by PETROBRAS. The SST data was processed by the NOAA/NASA AVHRR Oceans Pathfinder Program and distributed by NOAA.

References

Antonov, J. I., D. Seidov, T. P. Boyer, R. A. Locarnini, A. V. Mishonov, H. E. Garcia, O. K. Baranova, M. M. Zweng, and D. R. Johnson (2010), *World Ocean Atlas 2009*, Volume 2: Salinity. edited by S. Levitus, NOAA Atlas NESDIS 69, U.S. Government Printing Office, Washington, D.C., p. 184.

Bretherton, F. P. (1966), Critical layer instability in baroclinic flows, *Q. J. R. Meteorol. Soc.*, *92*(393), 325–334, doi:10.1002/qj.49709239302.

da Silveira, I. C. A., W. S. Brown, and G. R. Flierl (2000), Dynamics of the North Brazil current retroflection from the WESTRAX observations, *J. Geophys. Res.*, *105*(C12), 28,559–28,583.

da Silveira, I. C. A., J. A. M. Lima, A. C. K. Schmidt, W. Ceccopieri, A. Sartori, C. P. F. Franscisco, and R. F. C. Fontes (2008), Is the meander growth in the Brazil Current system off Southeast Brazil due to baroclinic instability?, *Dyn. Atmos. Oceans*, *45*(3–4), 187–207, doi:10.1016/j.dynatmoce.2008.01.002.

Dewar, W. K. (1998), Topography and barotropic transport control by bottom friction, *J. Mar. Res.*, *56*, 295–328.

Emery, W., and R. Thomson (2001), *Data Analysis Methods in Physical Oceanography*, Elsevier, Amsterdam, The Netherlands.

Ferrari, R., and C. Wunsch (2010), The distribution of eddy kinetic and potential energies in the global ocean, *Tellus A*, *62*(2), 92–108, doi:10.1111/j.1600-0870.2009.00432.x.

Fu, L. L., and G. R. Flierl (1980), Nonlinear energy and enstrophy transfers in a realistically stratified ocean, *Dyn. Atmos. Oceans*, *4*(4), 219–246.

Held, I. M., R. T. Pierrehumbert, S. T. Garner, and K. L. Swason (1995), Surface quasi-geostrophic dynamics, *J. Fluid Mech.*, *282*, 1–20.

Isachsen, P. E. (2011), Baroclinic instability and eddy tracer transport across sloping bottom topography: How well does a modified Eady model do in primitive equation simulations?, *Ocean Modell.*, *39*, 183–199.

Isern-Fontanet, J., B. Chapron, G. Lapeyre, and P. Klein (2006), Potential use of microwave sea surface temperatures for the estimation of ocean currents, *Geophys. Res. Lett.*, *33*, L24608, doi:10.1029/2006GL027801.

Isern-Fontanet, J., G. Lapeyre, P. Klein, B. Chapron, and M. W. Hecht (2008), Three-dimensional reconstruction of oceanic mesoscale currents from surface information, *J. Geophys. Res.*, *113*, 1–17, doi:10.1029/2007JC004692.

Kundu, P. K., J. S. Allen, and R. L. Smith (1975), Modal decomposition of the velocity field near the Oregon coast, *J. Phys. Oceanogr.*, *5*, 683–704.

LaCasce, J. H. (2012), Surface quasigeostrophic solutions and Baroclinic modes with exponential stratification, *J. Phys. Oceanogr.*, *42*(4), 569–580, doi:10.1175/JPO-D-11–0111.1.

LaCasce, J. H., and A. Mahadevan (2006), Estimating subsurface horizontal and vertical velocities from sea-surface temperature, *J. Mar. Res.*, *64*(5), 695–721, doi:10.1357/002224006779367267.

Lagerloef, G., et al. (2008), The AQUARIUS/SAC-D mission: Designed to meet the salinity remote-sensing challenge, *Oceanography*, *21*(1), 68–81.

Lapeyre, G. (2009), What vertical mode does the altimeter reflect? On the decomposition in baroclinic modes and on a surface-trapped mode, *J. Phys. Oceanogr.*, *39*(11), 2857–2874, doi:10.1175/2009JPO3968.1.

Lapeyre, G., and P. Klein (2006), Dynamics of the upper oceanic layers in terms of surface quasigeostrophy theory, *J. Phys. Oceanogr.*, *36*, 165–176.

Le Traon, P. Y., P. Klein, B. L. Hua, and G. Dibarboure (2008), Do altimeter wavenumber spectra agree with the interior or surface quasigeostrophic theory?, *J. Phys. Oceanogr.*, *38*(5), 1137–1142, doi:10.1175/2007JPO3806.1.

Locarnini, R. A., A. V. Mishonov, J. I. Antonov, T. P. Boyer, H. E. Garcia, O. K. Baranova, M. M. Zweng, and D. R. Johnson (2010), *World Ocean Atlas 2009*, Volume 1: Temperature. edited by S. Levitus, NOAA Atlas NESDIS 68, U.S. Government Printing Office, Washington, D.C., p. 184.

Müller, T. J., Y. Ikeda, N. Zangenberg, and L. V. Nonato (1998), Direct Measurements of western boundary currents off Brazil between 20° S and 28° S, *J. Geophys. Res.*, *103*(C3), 5429–5437.

Pedlosky, J. (1987), *Geophysical Fluid Dynamics*, Springer study ed., Spring-Verlag, New York.

Philander, S. G. H. (1978), Forced oceanic waves, *Rev. Geophys.*, *16*(1), 15–46.

Preisendorfer, R. (1988), *Principal Component Analysis in Meteorology and Oceanography, Dev. in Atmos. Sci. 17*, Elsevier, Amsterdam, The Netherlands.

Tulloch, R., J. Marshall, C. Hill, and K. S. Smith (2011), Scales, growth rates, and spectral fluxes of baroclinic instability in the ocean, *J. Phys. Oceanogr.*, *41*, 1057–1575.

Stammer, D. (1997), Global characteristics of ocean variability estimated from regional topex/poseidon altimeter measurements, *J. Phys. Oceanogr.*, *27*, 1743–1769.

Scott, R. B., and B. K. Arbic (2007), Spectral Energy Fluxes in geostrophic turbulence: Implications for ocean energetics, *J. Phys. Oceanogr.*, *37*(3), 673–688, doi:10.1175/JPO3027.1.

Scott, R. B., and D. G. Furnival (2012), assessment of traditional and new eigenfunction bases applied to extrapolation of surface geostrophic current time series to below the surface in an idealized primitive equation simulation, *J. Phys. Oceanogr.*, *42*(1), 165–178, doi:10.1175/2011JPO4523.1.

Szuts, Z. B., J. R. Blundell, M. P. Chidichimo, and J. Marotzke (2012), A vertical-mode decomposition to investigate low-frequency internal motion across the Atlantic at 26 N, *Ocean Sci.*, *8*(3), 345–367, doi:10.5194/os-8-345-2012.

Vallis, G. K. (2006), *Atmospheric and Oceanic Fluid Dynamics*, 745 pp., Cambridge Univ. Press, Cambridge, U. K.

Wang, D.-P., C. N. Flagg, K. Donohue, and H. T. Rossby (2010), Wavenumber spectrum in the Gulf stream from shipboard ADCP observations and comparison with altimetry measurements, *J. Phys. Oceanogr.*, *40*(4), 840–844, doi:10.1175/2009JPO4330.1.

Wunsch, C. (1997), The vertical partition of oceanic horizontal kinetic energy, *J. Phys. Oceanogr.*, *27*(1), 1770–1794.

Xu, Y., and L.-L. Fu (2011), Global variability of the wavenumber spectrum of oceanic mesoscale turbulence, *J. Phys. Oceanogr.*, *41*(4), 802–809, doi:10.1175/2010JPO4558.1.

Xu, Y., and L.-L. Fu (2012), The effects of altimeter instrument noise on the estimation of the wavenumber spectrum of sea surface height, *J. Phys. Oceanogr.*, *42*, 2229–2233, doi: 10.1175/JPO-D-12–0106.1.